GA–A26749

2D SOFT X-RAY SYSTEM ON DIII-D FOR IMAGING THE MAGNETIC TOPOLOGY IN THE PEDESTAL REGION

by

M.W. SHAFER, D.J. BATTAGLIA, E.A. UNTERBERG,
T.E. EVANS, D.L. HILLIS and R. MAINGI

JUNE 2010

GENERAL ATOMICS

DISCLAIMER

This report was prepared as an account of work sponsored by an agency of the United States Government. Neither the United States Government nor any agency thereof, nor any of their employees, makes any warranty, express or implied, or assumes any legal liability or responsibility for the accuracy, completeness, or usefulness of any information, apparatus, product, or process disclosed, or represents that its use would not infringe privately owned rights. Reference herein to any specific commercial product, process, or service by trade name, trademark, manufacturer, or otherwise, does not necessarily constitute or imply its endorsement, recommendation, or favoring by the United States Government or any agency thereof. The views and opinions of authors expressed herein do not necessarily state or reflect those of the United States Government or any agency thereof.

GA–A26749

2D SOFT X-RAY SYSTEM ON DIII-D FOR IMAGING THE MAGNETIC TOPOLOGY IN THE PEDESTAL REGION

by
M.W. SHAFER,* D.J. BATTAGLIA,* E.A. UNTERBERG,*
T.E. EVANS, D.L. HILLIS* and R. MAINGI*

This is a preprint of a paper to be presented at the 18th Topical Conference on High Temperature Plasma Diagnostics, May 16–20, 2010 in Wildwood, New Jersey and to be published in Review of Scientific Instruments.

*Oak Ridge National Laboratory, Oak Ridge, Tennessee USA

Work supported in part by
the U.S. Department of Energy
under DE-FC02-04ER54698
and DE-AC05-00OR22725

GENERAL ATOMICS ATOMICS PROJECT 30200
JUNE 2010

GENERAL ATOMICS

ABSTRACT

A new tangential 2D Soft X-Ray Imaging System (SXRIS) is being designed to examine the edge island structure in the lower X-point region of DIII-D. Plasma shielding and/or amplification of the calculated vacuum islands may play a role in the suppression of edge-localized modes via resonant magnetic perturbations (RMPs). The SXRIS is intended to improve the understanding of 3D phenomena associated with RMPs. This system utilizes a tangential view with a pinhole imaging system and spectral filtering with beryllium foils. SXR emission is chosen to avoid line radiation and allow suitable signal at the top of a H-mode pedestal where $T_e \sim 1$–2 keV. A synthetic diagnostic calculation based on 3D SXR emissivity estimates is used to help assess signal levels and resolution of the design. A signal-to-noise ratio of 10 at 1 cm resolution is expected for the perturbed signals, which is sufficient to resolve most of the predicted vacuum island sizes.

I. INTRODUCTION

Edge localized modes (ELMs) expel particles and energy, which can damage plasma-facing components. This is an important issue for future devices, such as ITER. The application of resonant magnetic perturbations (RMPs) can be used to completely suppress ELMs.[1] This is thought to stabilize ELMs by relaxing the sharp H-mode pedestal profiles to below the peeling-ballooning limit. Vacuum field modeling of the pedestal region suggests an increase in stochasticity and island overlap from RMPs, which may explain the stabilizing mechanism. However, the physical process is not fully understood. The plasma response to these vacuum fields is a key issue. Measurements of the island structure could provide a crucial link to the validity of vacuum models. Conversely, measurements could also show evidence that a better estimation of the plasma response is necessary to complete the ELM suppression picture.

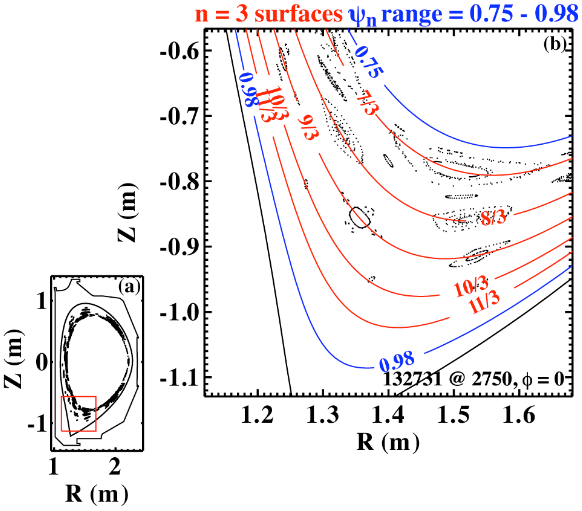

FIG. 1. (a) Radial-poloidal cross-section with island Poincaré points via vacuum field line tracing, and (b) an expanded view from the red box in (a).

A 2D tangential pinhole Soft X-Ray Imaging System (SXRIS) is proposed for DIII-D to examine these models. SXR imaging on tokamaks and stellarators has been used for many years.[2–5] More specifically, tangential SXR imaging has been recently used to image large rotating core islands on LHD and TEXTOR.[6] Islands flatten photon emissions locally to provide imaging contrast. Tomographic inversion techniques were used to isolate these core modes.[6] The SXRIS diagnostic on DIII-D intends to image small islands produced by non-axisymmetric perturbation coils as opposed to rotating MHD modes that are found in the edge region ($0.75 < \psi_n < 0.98$) near the lower X-point. The X-point region is chosen because islands are naturally larger due to the flux expansion at the poloidal field null.

ELM suppression on DIII-D is achieved using n=3 RMPs, where n refers to the toroidal mode number. Vacuum field modeling using the TRIP3D code[7] is shown in Fig. 1 for discharge with applied RMPs. The red box in Fig. 1(a) corresponds to the field-of-view for the proposed camera at the tangency radius. Figure 1(b) is an enlarged plot of this region. This figure shows the sizes of the islands vary from 1–20 cm from the 10/3 (m/n) island chain to the 7/3 island chain in the edge region of the lower X-point. The higher level of stochasticity toward the edge reduces the size of islands in this region. A diagnostic resolution of less than 1 cm is therefore desired. The estimated resolution based on modeling from Section III indicates 1 cm resolution is available.

II. SXRIS DESIGN

The SXR spectral region is chosen to avoid contamination of low-temperature edge spectral emission in the divertor region. In some cases, it is possible to image localized coherent structures in the visible spectrum that oscillate or rotate in the field of view at discrete frequencies. Frequency filtering can be used as a means to discriminate against light contamination.[8] However, the application of RMPs on DIII-D is currently restricted to static perturbations without the ability to rotate. In tokamak coordinates, (R,Z,ϕ), the local SXR emission is given by:[2]

$$\frac{dP}{dh\nu} \sim \frac{Z_{eff}\, n_e^2}{\sqrt{T_e}}\, e^{-\frac{h\nu}{kT_e}} \quad ,$$

where n_e (R,Z,ϕ) is the electron density, T_e (R,Z,ϕ) is the electron temperature, Z_{eff} (R,Z,ϕ) is effective atomic number, hν is the emitted photon, and k is Boltzmann's constant. This emission is dominated by Bremsstrahlung and recombination radiation of the thermal electrons.[2] The flattening in T_e (R,Z,ϕ) and n_e (R,Z,ϕ) due to the island structure leads to a local flattening of the SXR emission that produces the imaging contrast.

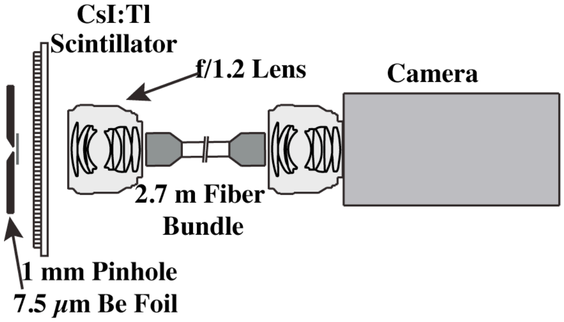

FIG. 2. Diagram of pinhole Soft X-Ray Imaging System proposed for DIII-D.

A diagnostic schematic is shown in Fig. 2. The system relies on pinhole imaging to a fast and efficient scintillator. The image is transferred out of vacuum to a camera in the visible spectrum. Each component in the optical train reduces the overall x-ray to electron efficiency. The estimated efficiencies are shown in Table I. The components are described below.

Table I
System Efficiency

Element	Photon Budget
CsI:Tl Scintillator Efficiency (number visible photons/1 keV x-ray)[9]	35
Lens Coupling	0.03
Fiber Transmission @ 550 nm[10]	0.34
Quantum Efficiency	0.3

X-ray Sensitivity	0.11 electrons/ 1 keV x-ray

A single pinhole of 1 mm diameter is used as a balance between spatial resolution and étendue. A single 7.5 μm Be foil is similarly chosen to maintain significant throughput, while removing most emission outside $\psi_n \sim 0.98$. The design does not incorporate variable pinhole or foil thickness due to the compact requirements for the DIII-D vessel. The effect of the pinhole size on the spatial resolution is discussed further in the next section.

The scintillator is chosen to be thallium-doped cesium iodide (CsI:Tl) and will be deposited onto a glass window, located 20 cm from the pinhole. CsI:Tl was chosen because the decay time (≤5 μs) is comparable to the common P43 phosphor (Gd_2O_2S:Tb, 4–7 μs), while having a photon conversion efficiency of ~4 times greater.[9] The P45 phosphor (Y_2O_2S:Tb) provides even better efficiency than CsI:Tl (~2.5x more), but at a much slower decay time of 1.5 ms.[9] Furthermore, CsI:Tl is approximately 8 times more efficient than the fast P47 scintillator (Y_2SiO_5:Ce, ~0.1 μs). The emission of CsI:Tl is centered at 550 nm, which is ideal for transmission with most optical components. The CsI:Tl conversion efficiency was measured to be ~35 photoelectrons per x-ray photon at 1 keV.[9] This conversion efficiency is energy dependent and decreases with lower x-ray energy.

The scintillator will be imaged with a commercially available f/1.2 imaging lens onto a coherent fiber bundle (Schott IG-163).[10] The fiber bundle is necessary to isolate the camera from the machine and appropriately shield from the radiation produced in the D-D plasmas. The fiber transmission is roughly 35% at 550 nm. Lens imaging is necessary given the port and size constraints. This reduces the light flux by 97% due to the need to de-magnify the image onto the fiber bundle. The resolution of the fiber bundle (~50 lp/mm) is sufficient for these measurements considering image demagnification.

The camera is chosen to be the 14-bit CMOS Phantom v7.3 with 800x600 22 μm pixels. A CMOS-based camera is preferred over a CCD-based camera because it is less sensitive to neutron radiation and can achieve higher full sensor frame-rates. This camera has a quantum efficiency ~30% (compared to >60% in fast CCD-based cameras). Integration time will be a key factor to obtain sufficient signal levels.

From Table I, approximately 10 x-rays at 1 keV are needed to produce one electron on the camera sensor. A large part of this reduction is the lack of direct imaging that is found in other designs.[5,6] The system is modeled to estimate realistic signal strengths in the next section.

III. SIGNAL-TO-NOISE RATIO ESTIMATION

A synthetic diagnostic approach is used to estimate signal strength of the diagnostic. The model used here is described in Ref. 11 (in this issue). It combines a 3D SXR emissivity calculation based on the experimentally measured plasma temperature, density, and impurity concentration and a pencil-line approximation to calculate the line-of-sight integration of each pixel with a Be filter.

The 3D fields of temperature, density, and impurity concentration can be approximated via multiple sources. One method uses the vacuum models to map out field line positions and use these mappings to project equilibrium quantities. Here, the initial value of ψ_n for a given field line is mapped every 2 deg for 200 toroidal revolutions where the (R,Z,φ) values are recorded. The experimental 1D profiles of n_e, T_e, and Z_{eff} versus ψ_n are then mapped to the 3D (R,Z,φ) positions. This method relies on the basic assumption that parallel transport is much greater than perpendicular transport. This is a reasonable assumption for these studies and compares well to the structure predicted by EMC3-EIRENE,[12] which is a self-consistent edge fluid transport code with recycling and neutral transport.

A single toroidal slice using this method is shown in Fig. 3(a). The island structure flattens the emissivity in several locations. A simulated camera image is shown in Fig. 3(b). The raw image shows little evidence of island structure. A full 2D inversion is needed to quantitatively identify the islands.[6] Techniques are under development and will be documented in a future publication.

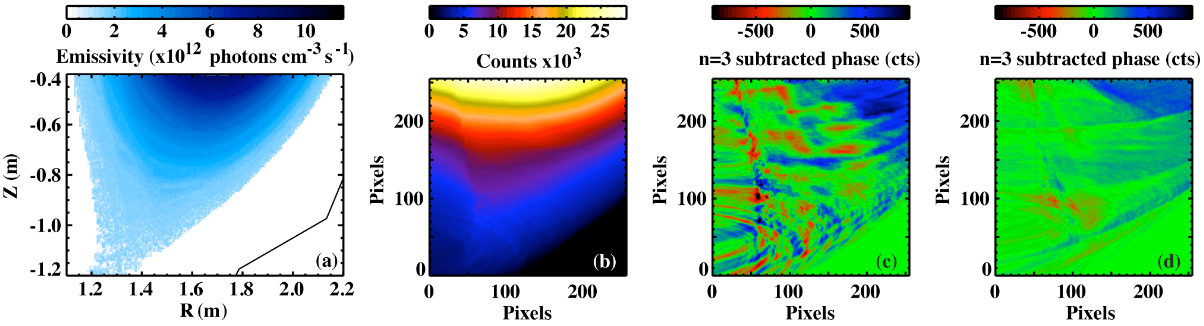

FIG. 3. (a) 2D SXR emissivity at tangency radius, (b) simulated camera image with synthetic diagnostic, (c) n=3 dominant component via out-of-phase (60 deg) subtracted image, and (d) out-of-phase (60 deg) subtracted image with artificially suppressed n=3 RMP.

Nonetheless, a qualitative understanding of the SXR perturbation image from the island structure is still possible without an inversion and was used in this study for the SXRIS design. The n=3 (120 deg) components can still be isolated by subtracting the out-of-phase image, or an image with the perturbation phase-shifted by 60 deg. The RMP can be configured in this way with the coil setup on DIII-D. The n=3 islands rotate poloidally with this phase shift such that the X-point and the O-point are swapped. Ideally, this subtraction would show a flattened region at the center of the island and peaking at the edge of the islands. However, because shaping complicates the island structure, the enhancement of the signal is not this straightforward.

The out-of-phase subtracted image is shown in Fig. 3(c). This image is dominated by n=3 components, but still contains remnant effects of other toroidal harmonics and boundary perturbations. The n=3 component represents ~5% of the total signal. The presence of the n=3 components can be confirmed by comparing this image to one with no n=3 RMPs. This is shown in Fig. 3(d), where a similarly phase-subtracted image is shown with the n=3 RMP coil currents set to zero for the vacuum modeling. The lack of structure in this image compared to Fig. 3(c) indicates the presence of n=3 islands with the RMP applied and that these islands are detectable based on this modeling. Structure in Fig. 3(d) still exists from error fields, which is predominantly n=1. There are also artifacts from this subtraction method.

The perturbed structure is used to estimate the signal-to-noise ratio (SNR). The RMS value of the central region in the perturbed image is taken to be the signal. The read noise is ~20 e^{-}/pixel (provided by manufacturer) and the dark noise is assumed to be 1000 e^{-}/pixel/s. The SNR is calculated via the ratio of the signal to the combination of shot, read, and dark noise.[13]

The SNR and spatial resolution are a trade-off. A larger pinhole allows more light and 0enhances the SNR, but reduces the spatial resolution. This effect is illustrated in Fig. 4.

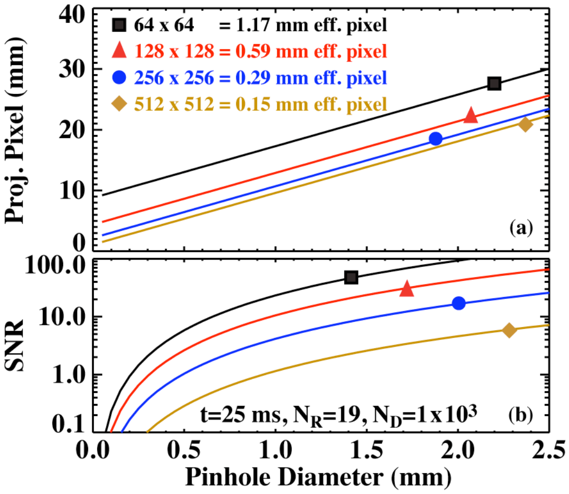

FIG. 4. (a) Projected pixel size at tangency radius for four different effective pixel sizes, which correspond to camera binning options listed in the legend and (b) the SNR.

The 7.5 cm^2 scintillator is divided up into "effective pixels" that are then imaged onto the camera. In this test, the effective pixel size is essentially controlled by the camera via binning and the size of the scintillator. Therefore, more binning will increase the effective pixel size. The projected pixel sizes at the tangency radius are shown in Fig. 4(a) for four sets of binning options (64x64, 128x128, 256x256, 512x512). This is a geometric calculation to represent the spatial resolution, but does not account for line integral effects. Sub-centimeter resolution is only available for small effective pixels and small pinhole diameters. Eventually, the resolution of infinitesimally small pixels is limited by the pinhole diameter.

The SNR is shown in Fig. 4(b). For good SNR (>10), a larger pinhole and pixel sizes are needed. A 1 mm pinhole with either a 128x128 or 256x256 effective pixel array is a good comprise between SNR and resolution. This provides a combination ~1 cm resolution and a SNR ~ 10. An integration time of 25 ms is used for this test to obtain the sufficient SNR.

In summary, the simulations above show the estimated signal strengths (SNR ~ 10) and resolution (1 cm). Based on these estimates, the SXRIS will have the appropriate flexibility to image islands at a larger normalized radius (i.e., the 7/3 to 11/3 chains in the region: $0.9 < \psi_n < 0.98$). This should aid the understanding of RMPs on ELMs by providing crucial internal measurements in the plasma edge region.

REFERENCES

[1] T. E. Evans, R. A. Moyer, P. R. Thomas, J. G. Watkins, T. H. Osborne, J. A. Boedo, E. J. Doyle, M. E. Fenstermacher, K. H. Finken, R. J. Groebner, M. Groth, J. H. Harris, R. J. La Haye, C. J. Lasnier, S. Masuzaki, N. Ohyabu, D. Pretty, T. L. Rhodes, H. Reimerdes, D. L. Rudakov, M. J. Schaffer, G. Wang, and L. Zeng, Phys. Rev. Lett. **92**, 235003 (2004).

[2] S. von Goeler, R. Kaita, M. Bitter, G. Fuchs, M. Poier, G. Bertschinger, H. R. Koslowski, K. Toi, S. Ohdachi, and A. Donne, Rev. Sci. Instrum. **70**, 599 (1999).

[3] K. Tritz, R. Fonck, M. Reinke, and G. Winz, Rev. Sci. Instrum. **74**, 2161 (2003).

[4] S. Ohdachi, K. Toi, G. Fuchs, S. von Goeler, and S. Yamamoto, Rev. Sci. Instrum. **74**, 2136 (2003).

[5] B. C. Stratton, R. Feder, S. von Goeler, G. F. Renda, V. J. Mastrocola, and J. L. Lowrance, Rev. Sci. Instrum. **75**, 3959 (2004).

[6] S. Ohdachi, K. Toi, G. Fuchs, TEXTOR team and LHD experimental group, Plasma Sci. Technol. **8**, 45 (2006).

[7] T. E. Evans, R. A. Moyer, and P. Monat, Phys. Plasmas **9**, 4957 (2002).

[8] J. H. Yu and M. A. Van Zeeland, Rev. Sci. Instrum. **79**, 10F516 (2008).

[9] L. F. Delgado-Aparicio, D. Stutman, K. Tritz, R. Vero, M. Finkenthal, G. Suliman, R. Kaita, R. Majeski, B. Stratton, L. Roquemore, and C. Tarrio, Appl. Opt. **46** 6069 (2007).

[10] SCHOTT North America, Inc., http://www.us.schott.com

[11] D. J. Battaglia, M. W. Shafer, E. A. Unterberg, B. C. Stratton, D. L. Hillis, and R. Maingi, submitted to Rev. Sci. Instrum. (these proceedings).

[12] H. Frerichs, D. Reiter, O. Schmitz, T. E. Evans, and Y. Feng, Nucl. Fusion **50**, 034004 (2010).

[13] S. B. Howel, *Handbook of CCD Astronomy* (Cambridge University Press, 2000).

ACKNOWLEDGMENT

This work supported in part by the U.S. Department of Energy under DE-AC05-00OR22725 and DE-FC02-04ER54698.